Visualization and PIV Measurements of the Transonic Flow around the Leading Edge of an eroded Fan Airfoil

Joachim Klinner*, Alexander Hergt, Manfred Beversdorff, Christian Willert

DLR Institute of Propulsion Technology, German Aerospace Center, 51170 Köln, Germany
* correspondent author: Joachim.klinner@dlr.de

Abstract The influence of blade deterioration on the time-averaged and instantaneous flow around a fan airfoil is investigated by PIV, schlieren imaging and high speed shock-shadowgraphs in a transonic cascade windtunnel. In addition to a global characterization of the time-averaged flow using PIV, the instantaneous passage shock position was extracted from single shot PIV measurements by matching the tracer velocity across the normal shock with an exponential fit. From this the relaxation time of paraffine-ethanol seeding was verified to have a response time in the sub-microsecond range. The instantaneous shock positions, defined by the onset of the exponential decay, are assigned to a probability density distribution in order to obtain the average position and the width of fluctuations. Finally the distributions from the generic blunted edge geometry and the unaffected reference geometry are compared under near stall and under choked conditions. At similar back-pressure conditions the passage shock of the blunted edge geometry is located further upstream in comparison to the reference geometry. The amplitude of shock fluttering is significantly higher for the blunted edge. In order to extract the frequency range of the shock motion the direct shadow of the shock wave was tracked in high-speed shadowgraphs and spectrally analyzed. A comparison of the power spectra of the shock motion indicates that under choked conditions the blunted edge geometry exhibits a more continuous spectrum with a broader frequency range. The paper discusses details on the experimental implementation such as a specifically designed purged light sheet probe.

1. Introduction

The optimization of aero engine fan maintenance and overhaul requires a detailed knowledge of the influence of blade deterioration on the transonic flow around the airfoil. The leading edge geometry of the fan airfoil has direct influence on the mass flow capacity and the stagnation pressure losses across the stage. On the other hand the leading edge of a fan blade is the most affected part since it has a high probability of high momentum, foreign particle impact during take off and landing. Typical long-term erosion damages can lead to a blunted edge as indicated in Fig. 1.

To study the influence of blade erosion on aerodynamic performance experimental investigations were carried out in a transonic cascade wind tunnel (TGK) at M_1=1.25 at the aerodynamic design point (ADP) with minimum losses and under off-design conditions (OFD) near stall. The geometry of the cascade represents a cut at 85 % of blade height. The generic eroded geometry used in the experiments has a leading edge reduction of 1.1 % of the chord-length.

The transonic flow field of both geometries was first visualized by schlieren imaging where it became apparent that at ADP conditions the passage shock is located at a certain downstream distance with respect to the leading edge while it is detached from the leading edge at near stall conditions. At certain operation conditions the shock position fluctuates several mm around an average position due to its interaction with the blade suction side boundary layer and due to back pressure fluctuations.

Planar 2C-PIV measurements are carried out at mid-span to measure the instantaneous and

averaged flow velocities around the leading edge and of the passage shock. The quality of PIV data obtained in a transonic investigation such as this one depends on the choice of tracer particles which should be able to follow decelerations across the shock with minimal decay. This is achieved by seeding the cascade wind tunnel with an atomized paraffine-ethanol mixture of which the ethanol part is evaporated upon injection into the tunnel. In order to determine whether the tracers follow the flow precisely, the particles' relaxation time [Melling 1997] is calculated from single shot PIV velocity profiles across the shock following the procedure proposed by [Ragni et al. 2011]. Statistical fluctuations are made visible by the statistical distribution of the relaxation time.

Numerical simulations of the transonic flow [Giebmanns et al 2012] predicted an upstream shift of the passage shock for the blunted edge geometry in comparison to the reference geometry at similar operating conditions. This shift is verified by the PIV measurements, from which the actual passage shock position of each single shot PIV measurement is extracted and subsequently averaged. The shock position in the PIV data is found by following certain streamlines and fitting the tracer velocity along the normal shock exponentially as described by [Ragni et al 2011]. The instantaneous shock position is defined by the onset of the exponential decay.

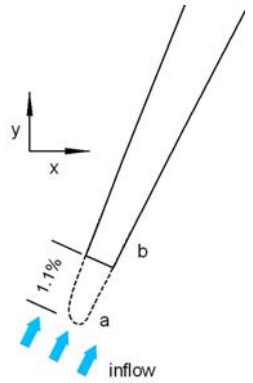

Fig. 1 Datum geometry (a) of the leading edge and generic blunted edge geometry (b)

The second part of the paper describes the analysis of the passage shock oscillations at high spatial and temporal resolution using high speed shadowgraphs and pulsed LED illumination at 20 kHz. Finally a frequency analysis of the high speed shadowgraphs of the passage shock is carried out to verify whether the shock fluttering is driven by dominant frequencies. Positions of the shock are extracted from the shadowgraphs by evaluating intensity gradients.

Aside from the description of data evaluation techniques and results obtained by PIV and visualization, the contribution describes experimental implementation issues such as the evaluation of tracer response and of the PIV light-sheet delivery via a purged optical probe.

2. Wind tunnel instrumentation and setting-up of operation conditions

The measurements are carried out in the transonic cascade wind tunnel (TGK) which is depicted in Fig. 3. The TGK is a closed loop, continuously running facility with a half-symmetrical nozzle and a variable test section by adjustment of the lower endwall. Additional suction capacities of the system allow the control of the side wall boundary layer in front of the cascade test section, in the upper and lower bypass channels as well as the transonic upper endwall. The suction capacities allow the adjustment of the static pressure across the channel height. Thereby, a homogeneous inflow according to an "infinite blade cascade" is achieved.

Furthermore additional suction slots in between the blades provide control of boundary layers on the side walls within the cascade passage. Thus, specific axial velocity density ratios (AVDR) at a controlled constriction can be adjusted. The necessary throttle system is combined with two tailboards hinged to the trailing edges of the outermost blades. The six cascade airfoils are supported by side walls made of acrylic (perspex) which provide optical access to the entire test section (see Fig. 2). Cascade parameter under design conditions can be found in Tab. 1. Visualization and PIV measurements are carried out in the passage between the third and forth airfoil.

Tab. 1 cascade geometry and flow parameter

Number of blades	6
Chord length	100 mm
Pitch to chord ratio	0.6895
Stagger angle	148.85°
Mach number	1.25
Reynolds number	$1.4x10^6$
Turbulence level	1%
Inlet total temperature	approx. 290 K

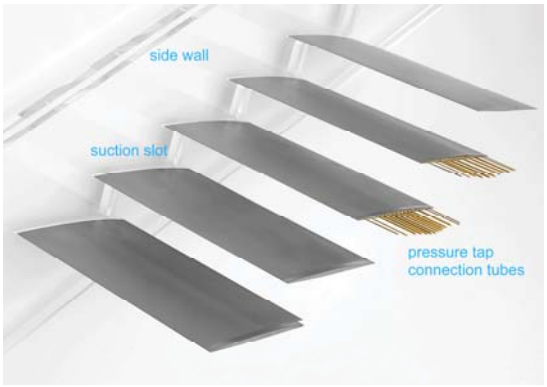

Fig. 2 Transonic cascade model

Static pressure tabs located at mid span on the suction and pressure sides of the third and forth airfoil enable the monitoring of the chord-wise pressure and isentropic Mach number distributions [Steinert et al 1992]. The traversal of a combined 3-hole and static pressure probe in the wake allow measurements of exit flow conditions. During the measurements of the datum and the blunted edge cascades, passage-to-passage flow periodicity is verified by traversing the wakes at mid span over the three middle passages as well as by measurement of the static pressure distribution across the inlet and outlet measurement plane.

Tab. 2 Inflow parameter and operation points (OP) of visualizations and PIV measurements according to Fig. 4

	β_1	Datum cascade OP	Blunted edge cascadeOP
Aerodynamic design point (ADP)	153.4°	54	56
Off-design point (OFD)	154.4°	76	89

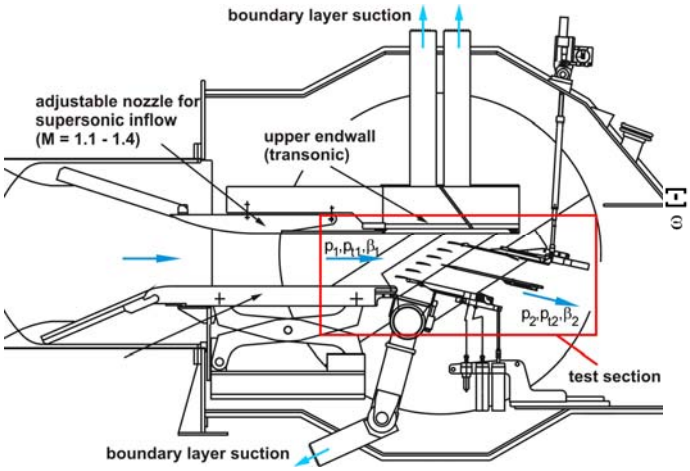

Fig. 3 The transonic cascade wind tunnel and operation parameters

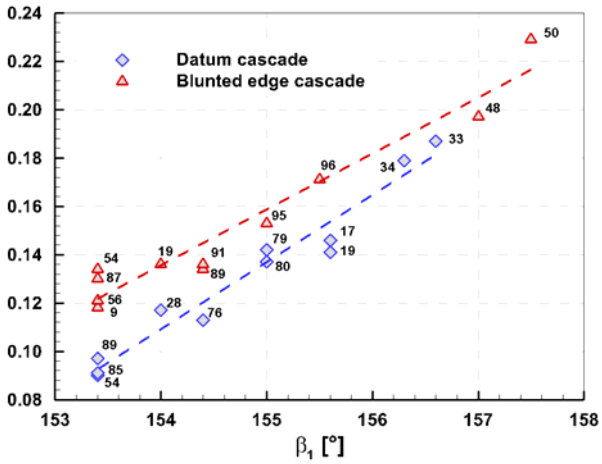

Fig. 4 Loss coefficient of the datum and blunted edge geometry at M_1=1.25

Flow conditions are adjusted in order to achieve a certain Mach number distribution on the airfoil pressure and suction sides which are predicted by numerical simulations at ADP and OFD conditions [Giebmanns et al 2012]. The pressure loss under certain operation conditions is characterized by the loss-coefficient [Cumpsty 1989]. The losses are conservatively averaged from pressure and temperature data and plotted against the inflow angle in Fig. 4**.** The visualizations and PIV measurements are carried out at operation points indicated in Tab. 2.

3. Experimental Methods

3.1. Schlieren and shadowgraphy instrumentation

The shock system within the five passages of the cascade is visualized by a conventional schlieren setup as described by [Settles 2006]. The light of a flash lamp at 160 ms pulse duration is collimated by a large concave mirror and therefore provides illumination of the entire cascade in order to check periodicity of the flow. A Nikon D200 is used for Schlieren imaging at a resolution of approximately 10 Pixel/mm and a region of 330 x 250 mm².

Passage shock oscillations are analyzed with high spatial and temporal resolution using high speed shadowgraphs obtained with pulsed LED back-illumination [Willert et al 2012]. The pulse duration is set to 2 µs at a repetition rate of 20 kHz. The light of a green Luminus SST-90 is collimated to approximately 100 mm diameter by a condenser lens. Images are recorded with a Fastcam Photron SA-5 at an image size of 704 x 520 Pixel. A highly magnified view of the fluctuating passage shock is imaged with a Nikkor Micro lens of f=200 mm and a resolution of approximately 47 Pixel/mm. This leads to a field of view (FOV) of 15 x 12 mm² which was aligned with the x-y-plane in Fig. 1. The f-stop is set to 5.6 resulting in a geometric-optical depth of field of approximately 1 mm when accepting a blur circle diameter of 2 pixel in the image.

3.2. PIV instrumentation

The wind tunnel imposes a number of restrictions for the placement of cameras for investigation and light sheet probe positioning. The existing optical access was originally designed for optimal schlieren imaging and requires additional optical access for the introduction of the light sheet normal to the viewing axis via light-sheet probe to enable 2C-PIV measurements.

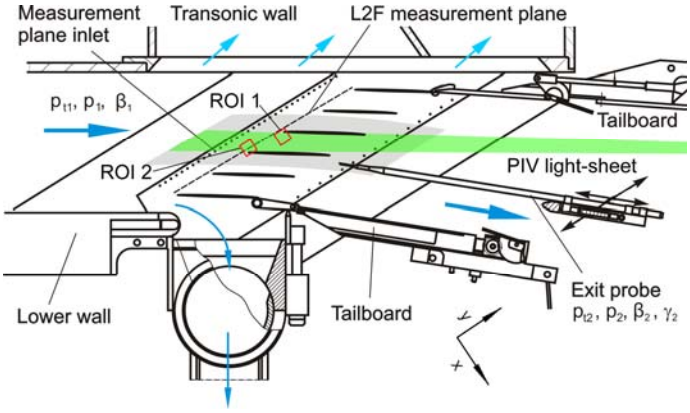

Fig. 5 PIV light-sheet orientation, ROI 1 and 2 are the PIV measurement regions at pressure and suction side of the airfoil

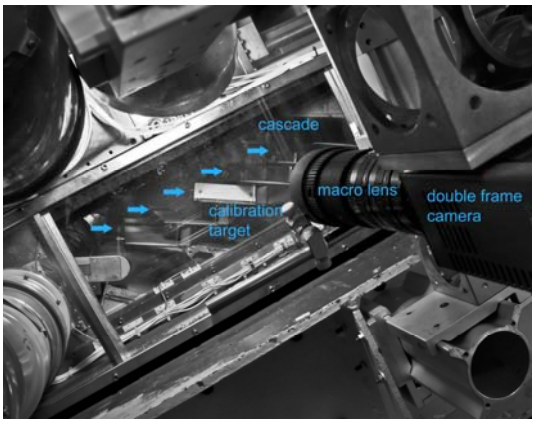

Fig. 6 PIV double frame camera orientation, flow direction as indicated

Fig. 5 shows a cross section of the transonic cascade windtunnel with light-sheet orientation. The PIV light sheet probe is introduced 550 mm downstream of the trailing edge of the middle cascade passage thus avoiding disturbances of the flow in upstream direction. Before entering the probe the laser-beam diameter is narrowed onto inner tube diameter of 14 mm by a lens doublet. This doublet also focuses the light-sheet waist through the tube at an overall distance of 1 m. Within the viewing area the sheet thickness is 0.5 mm at $1/e^2$ intensity level and has a light-sheet height of about 30 mm.

As the light-sheet probe is introduced downstream of the trailing edge, small cascade deflection angles at the transonic configuration lead to a high wind load on the probe at high Mach numbers (M_2=0.9). An earlier PIV campaign at M_1=1.28 showed that the tunnel flow carries significant amounts of rust particles whose high momentum leads to a fast erosion of the reflective coating on the 90 degree deflecting mirror at the tip of the light-sheet probe. As a result the light-sheet quality rapidly deteriorated to the point at which reliable PIV measurements were no longer possible.

To improve the protection of the mirror surface from incoming particles (rust) the probe tip was retrofitted with a Laval nozzle (c.f. Fig. 7) which redirects and accelerates the purge flow against the tunnel flow, ideally at supersonic speed. The inner contour of the nozzle was designed to match the beam shape based on beam profiler measurements. With this modification in place, PIV measurements can be performed for five hours of continuous operation of the cascade wind tunnel operation without noticeable damage to the mirror.

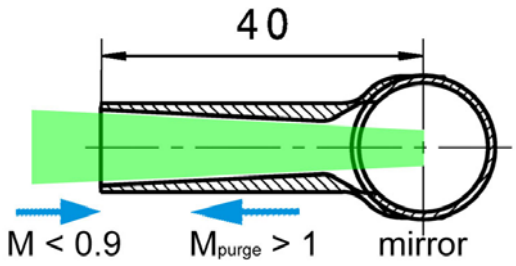

Fig. 7 Purging of PIV light-sheet probe

Laser energy of 25 mJ per pulse provides sufficient illumination by producing particle images with a signal of approximately 900 counts. The camera (PCO AG, pco.2000) is equipped with an f=180 mm lens at an effective f-number of 9.2 (M=0.66, nominal f-number=5.6). The camera observes tracer particles in a classical normal viewing arrangement (see Fig. 6). Camera and light-sheet are fixed on the inner sprocket. Therefore their orientation with respect to the model does not change when the inflow angle changes. The camera is fixed to the rotatable cascade support and thereby allows the direct comparison of PIV results at different inflow angles without requiring coordinate transformations.

The cascade wind tunnel facility is seeded with an atomized paraffine-ethanol mixture (1:2) dispersed by two atomizers. An impactor and a dryer between atomizer and test section limit the initial maximum droplet diameter to approximately 1 μm. Instead of using single seeding injectors the rake, which was found to introduce inhomogeneous particle distribution, a seeding injection rake of 300 x 300mm² is installed on the downstream of the screens within the settling chamber about 3 m upstream of the test section. This guaranteed a higher probability of sufficient and temporally constant tracer densities in the measurement domain even if the wake of the rake is temporally fluctuating. With this configuration number densities of 6-8 particle images per interrogation-window are obtained.

3.3. Determination of particle response and shock position

A precise determination of shock position requires particles which follow the flow with minimal delay. Following Stokes' drag law, [Melling 1997] showed that the normal velocity u of a single particle across the shock follows an exponential decay

$$\ln(u^*) = \ln\left(\frac{u-u_1}{u_0-u_1}\right) = -Kt = -\frac{t}{\tau} \quad (1)$$

Here u_0 is the normal tracer velocity upstream of the shock and u_1 the downstream velocity. A particle crossing the shock needs the relaxation time τ to decelerate to the 1/e part of the velocity step across the shock. The actual particle position x_n is obtained by integration of Eqn. 1. The distance which the particle moves within the relaxation time is given by the relaxation length ξ [Ragni et al 2011]

$$\xi = \tau\left[u_0 - \frac{u_0-u_1}{e}\right] \quad (2)$$

In order to infer the relaxation time of the droplet seeding, single shot PIV velocity profiles are extracted within a small stripe normal to the shock (see Fig. 8) and fitted against an exponential velocity profile according to Eqn. 1 (see Fig. 9). In contrast to an evaluation of velocity profiles from time-averaged PIV measurements this procedure allows the evaluation of statistical fluctuations of the relaxation time. Furthermore this approach does not require any compensation of shock or field of view (FOV) motion as it occurs in transonic cascade operation at high mass flows. Any movement of the FOV or of the leading edge due to acoustic excitation or mechanical vibration during the PIV campaign was monitored by the PIV camera and was found to be below 2 pixel. In contrast to the motion of the passage shock at M_1=1.25 covers an extensive cord-wise range of 4-8 mm or 350-700 Pixel.

In order to analyse fluctuations of shock fluttering, sequences of single shot velocity profiles are further used to determine the actual shock position. The chord wise shock position is given by the intersection of the linear slope with the upstream velocity level in the logarithmic scale representation of tracer velocity as proposed by [Schrijer and Scarano 2007] and [Ragni et al 2011] (see Fig. 9, middle). The width of spatial fluctuations around the average position is characterized by plotting the probability density distribution obtained from 1000 PIV measurements (see Fig. 13).

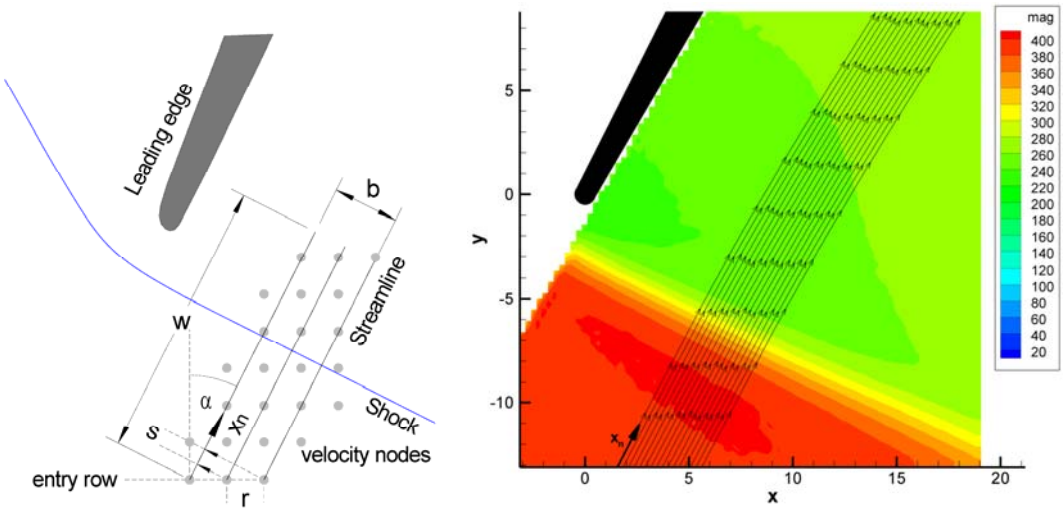

Fig. 8 Left: Extraction of stream wise velocities (not to scale); Right: Streamline region and orientation within averaged PIV data of the detached passage shock true to scale

3.4. Spatial and temporal resolution of PIV measurements

The temporal resolution of a PIV measurement is limited by the pulse separation which is set to 250 ns. This value is well below the expected relaxation time of about 2 µs as measured for typical DEHS droplet seeding [Ragni et al 2011]. Within this pulse separation displacements of 9 pixel are obtained at u_∞ (400 m/s).

The spatial resolution is limited by the interrogation window size which is set up according to available tracer image densities. This effect leads to a smoothing of the theoretical velocity decay which is apparent in the velocity profiles in Fig. 9 upstream of the shock. Each interrogation window covers a region of 0.54 x 0.54 mm² which is on the order of magnitude as the expected relaxation length of 0.7 mm (Eqn. 2 with τ=2 µs).

The accuracy of the velocity profile across the shock is further increased by spatial averaging of 16 velocity streamlines within a region of w=15.0 and b=3.6mm (see Fig. 8, left and right) at a PIV sampling distance of r=0.27 mm. The spatial averaged single shot velocity profile is therefore calculated from up to 800 velocity nodes within the stripe. Along x_n this corresponds to a maximum density of 53 PIV samples per mm.

Tab. 3 PIV parameter

Field of view [mm]/[pixel]	23 x 23 / 2048 x 2048
Magnification [-]/[pixel/mm]	0.65 / 88.6
Pulse delay [ns]	250
u_∞ [m/s]/[pixel]	400 / 8.8
Window size [mm]/[pixel]	0.54 x 0.54 / 48 x 48
Sampling [mm]/[pixel]	0.27 x 0.27 / 24 x 24
Interrogation method	Multi-grid + image deformation + window offset
Peak detection	Least squares Gauss fit (3 x 3)
Vector validation test / threshold	max. displacement / 16 px max. displacement diff. / 7 px normalized median / 7

3.5. Single shot PIV velocity extraction, normalization and fitting

The nodes along a streamline are found by starting from the entry row and by following the tangential velocity of each streamline at equidistant time steps. The orientation of each streamline is then linearly interpolated from the positions of these nodes. The average direction is given by α (see Fig. 8, left). In a sequence of 1000 single PIV measurements the tangent of α within the evaluated region was constant 0.509±0.007 (α=26.97°). The instantaneous velocity components along the linear streamline fit are bilinearly resampled between the two nearest columns in order to obtain values for each row. If one of the neighbours is an outlier the velocity value is rejected. Validation parameters to exclude outliers are listed in Tab. 3. The validation rate of all regarded velocity nodes within 1000 single shot PIV evaluations is 91%. All extracted single shot velocities of each streamline are finally projected onto the x_n axis with an offset of $s_i = i\ r\ \sin\alpha$.

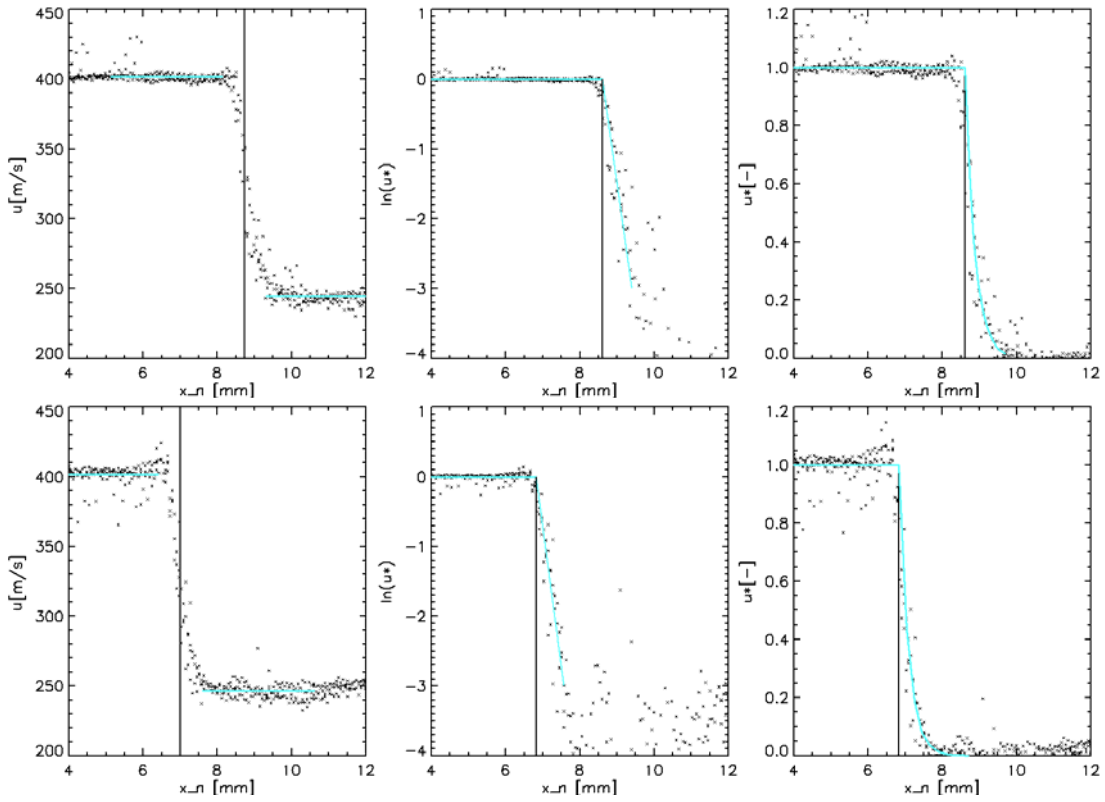

Fig. 9 Evaluation of normal velocity profiles along x_n of two instantaneous PIV measurements (top and bottom), left: pre estimation of shock position with u_0 and u_1 level, middle: normalized logarithmic representation, right: fitted velocity decay across the shock

The shock position within the spatially averaged velocity profile is estimated by the minimum of the velocity gradient along the profile (see Fig. 9, left). The velocities upstream and downstream of this shock position are averaged in a 3 mm region at 1 mm distance to the estimated shock position in order to obtain average values for u_0 and u_1. The velocity slope in the logarithmic representation was linear interpolated within a dynamic range of $\ln(u^*)$=-2.5…-0.5 (see Fig. 9, middle). Furthermore the valid Δx_n around the estimated shock position was preset with 1.4 mm. The final plot of the exponential tracer velocity decay is shown in Fig. 9, right.

3.6. Frequency analysis of shock fluttering using high-speed shadowgraphy

The shadowgraphs are median filtered with a 3 x 3 kernel in order to exclude hot and cold pixel defects of the CMOS camera sensor. The shock is located at pronounced intensity gradients in the single shot shadowgraph. Prior the shock detection, spatial inhomogeneities of the background illumination are compensated and the contrast of the shock-imposed gradients is enhanced. To do so the time-averaged intensity of each pixel is subtracted and then the difference is divided by the time-average. The time-average of pixel intensities, apart from the shock induced gradients at a framerate of 20 kHz, are rather constant and within a margin of ±1 % per pixel.

The orientation of the FOV of the high speed camera corresponds to the red box in Fig. 10, left. The intensity is averaged over 20 pixel rows along the normal passage shock to suppress camera noise. Image differentiation is carried out normal to the shock within a 3-connected neighbourhood. The local maxima of the squared derivation of the intensity are then validated by a certain threshold. Because the measurements are carried out at mid-span, the most downstream local maximum of the squared gradient is considered to be the shock position. An exemplary sequence of 15 consecutive shadowgraphs in Fig. 10, right shows the transient motion of the passage shock. The black vertical bar marks the detected shock position in each frame. Within a sequence of 30000 frames recorded at 20 kHz the width of the direct shadow image of the shock can vary between 3-7 pixel. At higher width the contrast is reduced. These effects lead to occasional detection faults within the shock width. Therefore the sequence of shock positions was median-filtered within a 3-neighbourhood prior to spectral analysis. The power spectrum of the entire record of 30000 frames deliveres rather noisy results which motivates the use of the averaging modified periodograms method [DeFatta et al. 1989]. This method is based on averaging the DFTs of a temporally sliding window of a fixed width and overlap. Here the window is weighted by a Hanning-function. Different window sizes up to 25 ms at different overlaps are tested. The spectral analysis and optimization of processing parameter is still in progress. Resulting power spectra of several row–wise shock detections are averaged to increase accuracy.

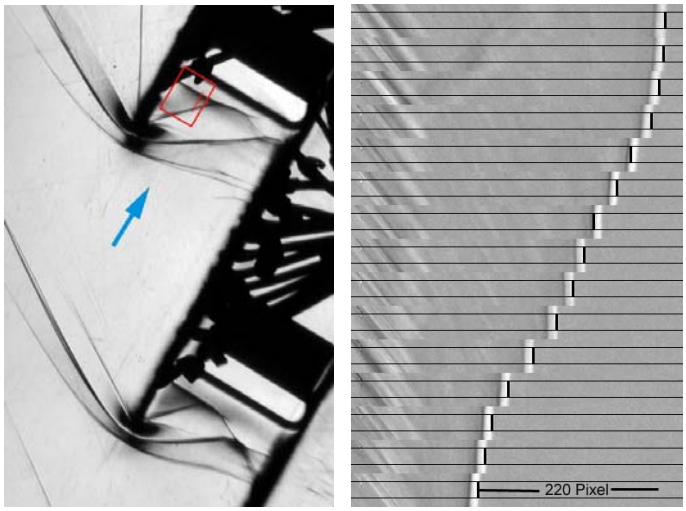

Fig. 10 Left: schlieren image near ADP conditions; Right: exemplary oscillation of the shock position along x_n in 15 consecutive shadowgraphs within the striped region

4. Discussion of Results

4.1. Response of Paraffine droplet seeding to the shock

The distribution of the probability density of particle relaxation time within a sequence of 918 validated PIV evaluations is depicted in Fig. 11. The average value is τ=0.77±0.15 µs which indicates an acceptable time response of the paraffine droplet seeding. Measured relaxation times reported from [Ragni et al 2011] are of τ = 1.92-2.02 µs measured for DEHS seeding dispersed by Laskin atomizer with 12 nozzles and of τ = 1.36-1.67 µs for TiO_2.solid particles of 50 nm primary crystal size dispersed by a fluidized bed seeder.

The characteristic relaxation length of tracer velocity deceleration to the 1/e part of the velocity gap across the normal shock is ξ = 0.23±0.045 mm.

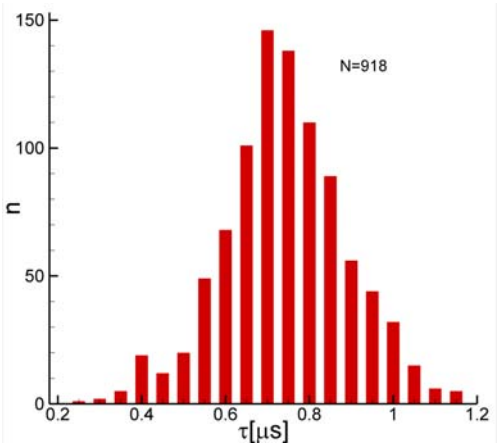

Fig. 11 Distribution of the relaxation time of paraffine-ethanol droplet aerosol

The average relaxation time across the shock can be used to infer the average particle droplet diameter. If small spherical droplets are assumed at, the modified Stokes' drag law can be applied [Melling 1986], [Scarano, Oudheusden 2003]. Based on a particle density of ρ_p=0.85 g/cm³ with the ethanol part fully evaporated and a maximum particle slip velocity of Δu=150 m/s this would lead to an average particle diameter of about d_p=0.4 µm.

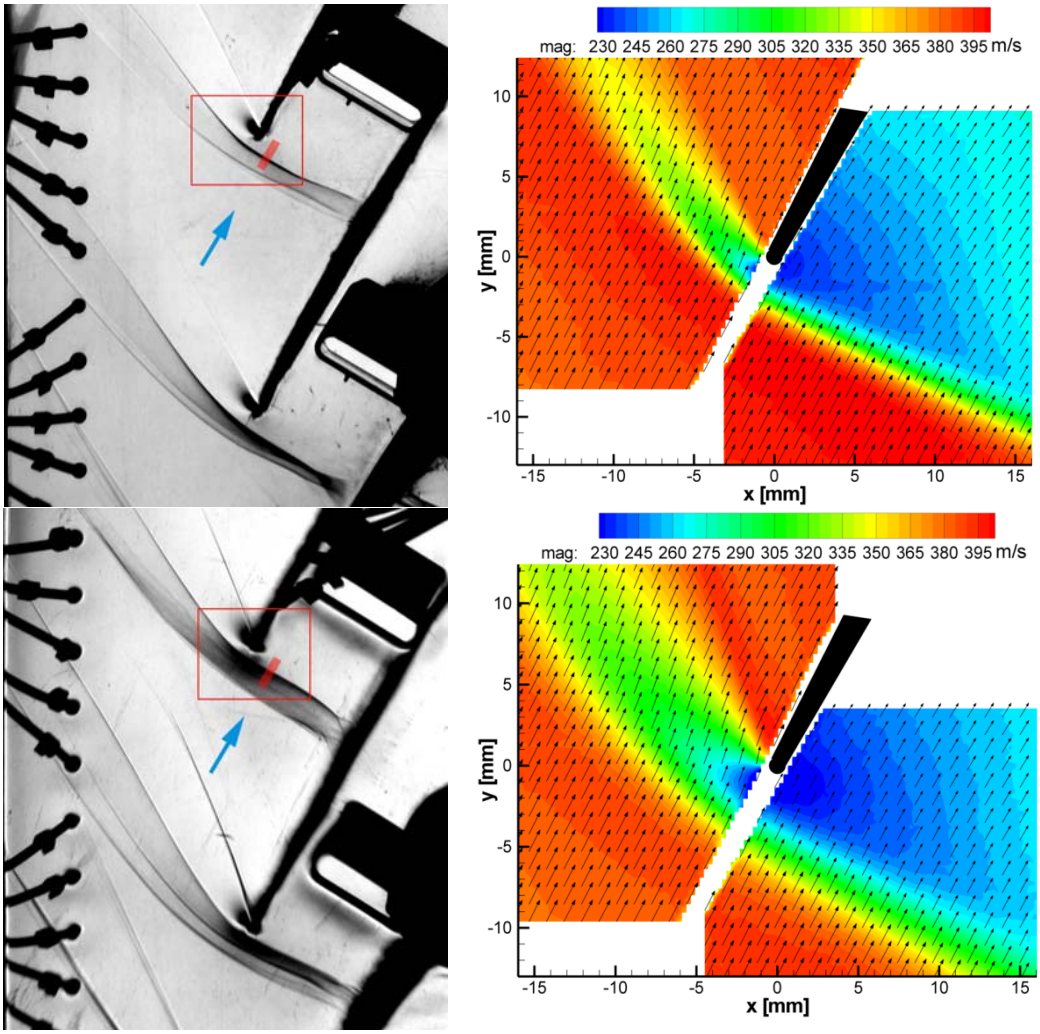

Fig. 12 Left: Schlieren images of the shock system of the reference cascade (top) and blunted edge cascade (bottom) near stall (OFD point); Right: Average Velocity fields (every forth vector plotted) according to the

region indicated by the red box

4.2. Comparison of the transonic flow field around the leading edge

Schlieren images and averaged PIV measurements of the flow field at off design conditions near stall are depicted in Fig. 12. The top row represents the datum cascade while the bottom row represents the blunted edge geometry. While the position of the detached shock in the single shot schlieren image looks similar, it is stronger and even more blurred for the blunted edge geometry. Furthermore the normal shock part has a greater extension. The blunted edge geometry shows a much stronger lip shock on the suction side. The averaged PIV velocities around the blunted edge confirm an second velocity decay due to the lip shock on the suction side and furthermore a stronger deflection in the vicinity of the leading edge at the suction side. The stronger lip shock of the blunted edge is caused by an intensified expansion flow.

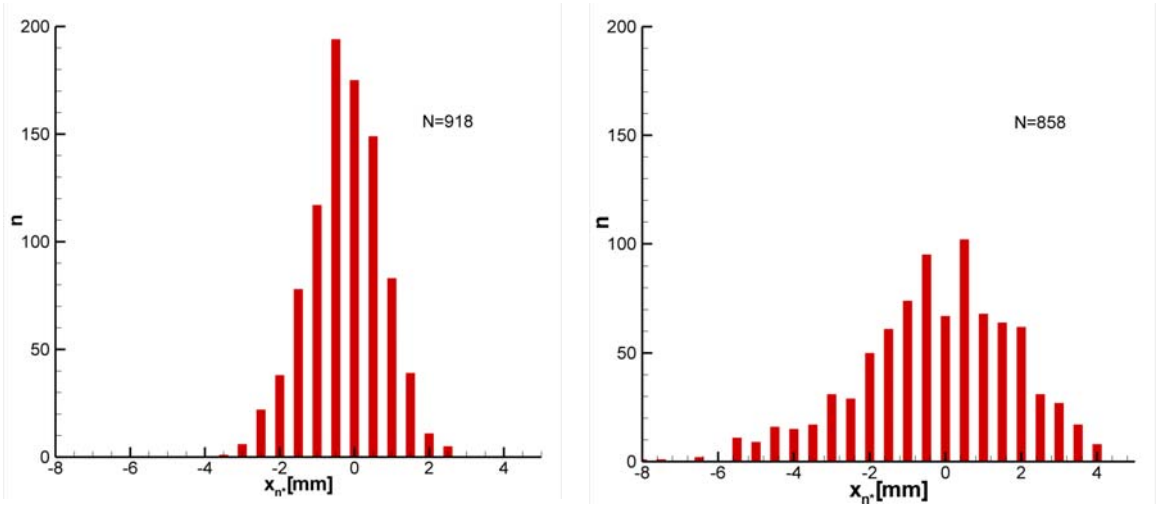

Fig. 13 Fluctuations around the average shock position along x_n near stall (OFD point) within the indicated stripe in the schlieren images in ; left: datum cascade; right: blunted edge cascade

The evaluation of single shot PIV measurements recover a wider spatial fluctuation of the detached passage shock along x_n for the blunted edge. Amplitudes of shock motion are doubled, which is confirmed by the statistical distribution of the shock position around the average position, shown in Fig. 13. In effect this leads to a stronger smoothing of the time-averaged PIV velocity gradients across the detached shock of the blunted edge geometry (Fig. 12, bottom right) in comparison to the reference edge (Fig. 12, top right). While the distribution of the shock position around the average is symmetric for the reference geometry, the shock of the blunted edge geometry shows higher amplitudes in upstream direction. Single shot PIV measurements also exhibit temporally stable flow acceleration upstream of the fluctuating shock.

In addition the detached passage shock is located further upstream of the blunted edge compared to the reference geometry at increased back pressure conditions (see Fig. 12, right). The same effect occurs under choked conditions and is confirmed by a numerical simulation and described in detail in [Giebmanns et al 2012]. This leads to an increased thickening of the boundary layer along the chord which in effect reduces the mass flow capacity of the cascade.

Fig. 14 shows a comparison of the power spectrum of shock motion for both geometries at the aerodynamic

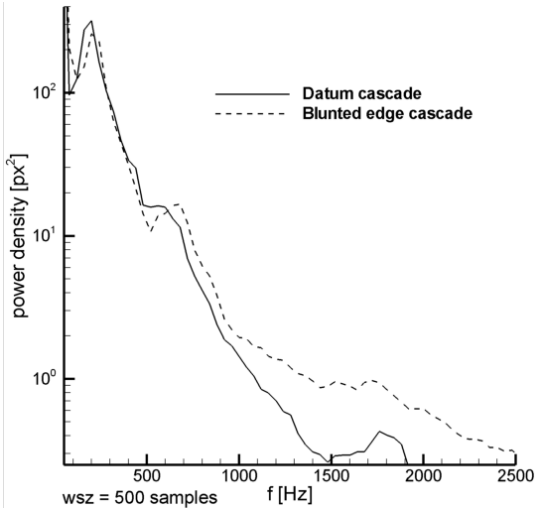

Fig. 14 Power spectrum of shock motion under choked conditions

design point. Here a window function of a width of 25 ms (500 samples) is applied. The entire sequence has a length of 30000 frames at 20 kHz. The shock motion of the blunted edge geometry contains higher frequencies, possibly due to higher turbulence. Both geometries show a peak at 200 Hz. The blunted edge power spectrum in addition shows a weak local peak at 700 Hz which corresponds to the oscillation of the passage shock in Fig. 10, right. More generally the motion of the passage shock due to boundary layer interaction is not affected by strong dominant frequencies.

Conclusions and outlook

This contribution described an experimental study aimed at investigating the influence of fan blade erosion on the transonic flow around the leading edge by schlieren imaging and PIV. Seeding for PIV was provided by an atomized ethanol paraffine mixture of which the ethanol evaporates upon injection into the tunnel. The resulting paraffine particles have response times in the sub-microsecond range which was verified through detailed analysis of the acquired PIV data.. The relaxation time was found to be τ=0.67 µs which corresponds to a characteristic distance of 0.23 mm which the particles need to decelerate by 63% of the velocity step across the normal shock.

The time-averaged PIV measurements show the stronger flow deflection in the vicinity of the leading edge at the suction side of the blunted edge and an intensified expansion flow. The eroded geometry therefore produces an additional abrupt velocity decay upstream of the bow shock due to a stronger lip shock on the suction side of the blunted edge. At equal back pressure conditions the average passage shock position on the suction side of the eroded airfoil is shifted significantly upstream in comparison to the shock position of the unaffected geometry. The evaluation of instantaneous shock positions from single shot PIV measurements additionally recover a doubled amplitude of fluctuations of the passage shock position at equal back pressure for the blunted edge. Further data analysis of PIV results will be conducted to validate simulations of the flow which are later needed to optimize the revision of the eroded fan blade geometry.

The power spectra of shock motion for both geometries show that the motion of the passage shock due to boundary layer interaction is not affected by strong dominant frequencies. The shock motion of the blunted edge geometry contains higher frequencies, possibly because the eroded geometry induces higher turbulences. The tracking of shock motion from direct shadow images of the shock wave requires further parameter optimization to improve the spatial resolution of shock position. One problem encountered here is the random broadening of the width of the direct shadow image within the image sequence which reduces the visibility of the shock. Furthermore, window size and overlap of the method of averaging modified periodograms have to be optimized.

Acknowledgements

The authors would like to thank Michael Schroll, Melanie Voges, Wolfgang Steinert and Sebastian Grund for the support during the PIV and high speed shadowgraph campaign. Part of the work reported in this paper is performed under the German Aviation Research Program (LuFo IV) and is funded in part by the Federal Ministry of Economics and Technology. In this context Lufthansa Technik AG is acknowledged for the good cooperation. Additional funding is provided by the EU-project AFDAR (Advanced Flow Diagnostics for Aeronautical Research, project no. 265695) of the 7th Framework Program whose support is gratefully acknowledged. Finally the authors would like to thank ANSYS for providing the hot geometry of the reference blade.

References

Cumpsty, N.A. (1989) Compressor aerodynamics. Longman Scientific & Technical Harlow, Essex, England

DeFatta D J, Lucas J G, Hodgkiss W S (1988) Digital Signal Processing. John Wiley & Sons, Inc. New York, NY

Giebmanns A, Schnell R, Steinert W, Hergt A, Nicke E, Werner-Spatz C (2012) Analyzing and Optimizing Geometrically Degraded Transonic Fan Blades By Means of 2D and 3D Simulations and Cascade Measurements. ASME Turbo Expo, Copenhagen, Denmark, June 11-15

Melling A (1997) Tracer particles and seeding for particle image velocimetry. Meas. Sci. Technol. 8, 1406-1416

Melling A (1986) Seeding gas flows for laser anemometry. Proceedings of the Conference on Advanced Instrumentation for Aero Engine Components, AGARD CP-399, 8.1

Ragni D, Schrijer F, van Oudheusden BW, Scarano F (2011): Particle tracer response across shocks measured by PIV. Exp Fluids. 50 (1), 53-64

Scarano F, van Oudheusden BW (2003) Planar velocity measurements of a two-dimensional compressible wake. Exp Fluids 34:430–441

Settles G S (2006): Schlieren & Shadowgraph Techniques. Springer Verlag, Berlin Heidelberg New York

Steinert W, Fuchs R and Starken H (1992) Inlet Flow Angle Determination of Transonic Compressor Cascade. Journal of Turbomachinery, ASME, 114(3), July, pp. 487-493.

Willert C, Mitchell D M, Soria J (2012) An assessment of high-power light-emitting diodes for high frame rate schlieren imaging. Exp Fluids, online first, DOI 10.1007/s00348-012-1297-1